

ANALYSIS OF DYNAMICS AND OPERATOR SPLITTING TECHNIQUES FOR TWO-PHASE FLOW WITH GRAVITY

KNUT-ANDREAS LIE, JOSTEIN R. NATVIG, AND HALVOR MØLL NILSEN

This paper is dedicated to the memory of Magne S. Espedal (1942–2010)

Abstract. We study the dynamics of two-phase flow with gravity and point out three different transport mechanisms: irrotational advection, solenoidal advection, and gravity segregation. Each term has specific mathematical properties that can be exploited by specialized numerical methods. We argue that to develop effective operator splitting methods, one needs to understand the interplay between these three mechanisms for the problem at hand.

Key Words. operator splitting, Helmholtz decomposition, porous media flow

1. Introduction

Numerical approximation of multiphase flow in heterogeneous reservoirs generally give rise to large systems of nonlinear equations that need to be solved in order to advance the solution forward in time. To a large extent, the success or failure of simulation development depend on the robustness and efficiency of the nonlinear solvers rather than the quality of the discretization. This has led to widespread use of fully implicit formulations which promise unconditional stability. In practical simulations, however, robust implementations of fully implicit schemes must limit the length of the time step, depending on the complexity of the grid, the geology, fluid physics, discretization scheme etc. With increasingly large and complex reservoir descriptions, there is a growing demand for faster yet stable and predictable simulation technology. To achieve higher efficiency in reservoir simulation technology, solvers tend to exploit special features of the flow physics and possibly use some form of sequential operator splitting.

The key idea of operator splitting for an evolutionary problem is to divide the model equations into a set of subequations that each model some parts of the overall dynamics that can be conquered using a simpler or more effective solution method. An approximation to the evolutionary solution is then constructed by solving the subequations independently, in sequence or parallel, and piecing the results together. Formally, we want to solve a Cauchy problem of the form

$$(1) \quad \frac{dQ}{dt} + \mathcal{A}(Q) = 0, \quad Q(0) = Q_0$$

where \mathcal{A} is an abstract and unspecified operator. The equation has the formal solution $Q(t) = \exp(-t\mathcal{A})Q_0$. Assume now that we can write $\mathcal{A} = \mathcal{A}_1 + \dots + \mathcal{A}_m$ in some natural way and that we know how to solve the sub-problems

$$(2) \quad \frac{dQ}{dt} + \mathcal{A}_j(Q) = 0, \quad j = 1, \dots, m$$

more effectively than solving (1). Introducing a time step Δt , and setting $t_n = n\Delta t$, the operator splitting can formally be written as

$$(3) \quad Q(t_{n+1}) = e^{-t_{n+1}\mathcal{A}}Q_0 \approx \left[e^{-\Delta t\mathcal{A}_m} \dots e^{-\Delta t\mathcal{A}_2} e^{-\Delta t\mathcal{A}_1} \right] Q(t_n).$$

Numerical methods are obtained by replacing the abstract operators $e^{-t\mathcal{A}_j}$ by numerical approximations. This way, one can combine numerical methods that have been developed to solve a particular class of evolutionary problems in a fairly straightforward manner, reusing specialized, highly efficient, and well-tested solvers. In particular, operator splitting enables easy replacement of one scheme with another scheme for the same elementary operator. Moreover, the use of operator splitting may also reduce memory requirements, increase the stability range, and even provide methods that are unconditionally stable.

One of the first operator splitting methods used within reservoir simulation, was the *alternating direction implicit* (ADI) method [29, 9], in which multi-dimensional flow problems were successfully reduced to repeated one-dimensional problems that could be effectively solved using the Thomas algorithm. Other examples of operator splitting include methods like IMPES, IMPSAT, sequential splitting, sequentially fully implicit, which all focus on splitting the computation of flow and transport in separate steps. Such a splitting has been an essential assumption for the development of specialized and highly efficient methods like streamline methods [8] and multiscale solvers [11]. In this paper, we will focus on another problem, namely the use of splitting for transport equations with a strong hyperbolic nature to enable the use of efficient advective solvers.

In general, there are often several ways to decompose an evolution operator. A good starting point is to have effective and specialized solvers for parts of the problem, e.g., an effective pressure solver, an effective solver for advective flow, etc. Designing an optimal solution strategy, however, will also require a good understanding of how the different physical effects act together to form the overall dynamics of the problem so that one can: (i) optimize the operator decomposition into 'clean' subproblems that can be solved as effectively as possible, and (ii) efficiently piece together the resulting sub-solutions without creating undesired artifacts in the approximate solution. Moreover, operator splitting can be used to accommodate the intuitive principle that each physical effect should (ideally) be evolved using its appropriate time constant.

Herein, we consider a common two-level operator-splitting method: first split the flow and transport equations, and then introduce a further operator splitting for the transport equation to enable the use of effective hyperbolic solvers for the advective part. Various splitting methods for the transport equation are analysed, both numerically and theoretically, by [14, 19], focusing in particular on the interaction of viscous and capillary forces. In the following, we will disregard capillary forces and instead focus on operator-splitting methods for problems involving only advective and gravitational forces.

As an example, consider streamline methods in which the pressure and velocity are computed on a grid and the transport of phases is computed along one-dimensional curves. The power of streamline methods is that the streamlines change slowly with time compared to the dynamics of saturation fronts. For advection-dominated problems, streamline methods has been proven to be (significantly) more efficient than conventional methods [2, 30, 8]. A different, but related, approach is to exploit the underlying direction of flow to construct nonlinear Gauss-Seidel type iterations for standard finite-volume discretizations [1, 22, 27, 28], which may

give up to two orders of magnitude reduction in run-time compared to standard methods.

Both these methods are based on two important assumptions: (i) that the characteristics of the hyperbolic system are always positive, and (ii) that the vector field is associated with potential flow. Both assumptions break down when gravity is included. One will then in general have both positive and negative characteristics and a rotational component in the velocity field. This leads to streamlines forming closed loops and large irreducible blocks in the nonlinear systems for finite-volume schemes [28] and can significantly deteriorate the efficiency of streamline and re-ordering methods, even if the solenoidal velocity component is orders of magnitude smaller than the advective part in most of the domain. In addition, the solenoidal part of the velocity field is moving with the fluid since it is governed by the density difference. In summary, our analysis will show that instead of splitting the transport into advection and gravity segregation, it is natural to consider three different contributions to the dynamics: irrotational advection, solenoidal advection, and gravity segregation.

The analysis naturally leads to a family of new splitting methods that isolates the rotational part of the velocity in a separate splitting step, thereby reducing its negative impact on the time step and the overall simulation efficiency. The new methods require an additional pressure solve with a different right-hand side to compute the solenoidal velocity, but the associated cost is low for many types of linear solvers since preprocessing, preconditioning, or factorizations of the coefficient matrix may be reused.

2. Discussion of dynamics

To keep the discussion as simple as possible, we consider incompressible flow of two immiscible fluids with different densities. The mathematical model is stated using a fractional flow formulation that separates the evolution into an elliptic flow equation for pressure and fluid velocity and a transport equation with strong hyperbolic characteristics for fluid saturations

$$(4) \quad \nabla \cdot \vec{v} = q, \quad \vec{v} + \lambda \mathbf{K} [\nabla p - (\lambda_w \rho_w + \lambda_n \rho_n) \vec{g}] = 0$$

$$(5) \quad \phi \frac{\partial S_w}{\partial t} + \nabla f_w (\vec{v} + \lambda_n (\rho_w - \rho_n) \mathbf{K} \vec{g}) = q_w.$$

Here, p is the fluid pressure, \vec{v} is the total Darcy velocity, S is the saturation of the wetting phase, \mathbf{K} and ϕ are the absolute permeability and porosity, respectively, ρ_α are the phase densities of the wetting (w) and non-wetting (n) phase, λ_α denote phase mobilities, and \vec{g} is the acceleration of gravity. The total mobility, fractional flow, and source terms are defined by $\lambda = \lambda_w + \lambda_n$, $f = \lambda_w / \lambda$, and $q = q_w + q_n$, respectively. Throughout this paper, we use no-flow boundary conditions for each of the equations in (4) and (5). In the following, we will assume that the flow equation (4) can be solved (e.g., by a finite-volume method) to give a flux field with one scalar value v_{ij} associated with each interface between two cells i and j . If \vec{g} is set to zero in (5), the transport equation has only positive characteristics and can be discretized using a standard single-point upwind discretization

$$(6) \quad \Phi(\mathbf{S}^{n+1} - \mathbf{S}^n) + \Delta t \mathbf{V} \mathbf{f}(\mathbf{S}^{n+1}) = \mathbf{q}.$$

Here, $\Phi = \text{diag}(\phi_i)$ where ϕ_i is the porosity in cell i , \mathbf{S} is the vectors of volume-average saturations per cell, \mathbf{f} the vector of fractional flow values per cell, \mathbf{q} the

fluid sources per cell, and \mathbf{V} is the so-called upwind flux matrix given by

$$(7) \quad \mathbf{V}_{ij} = \begin{cases} \min(v_{ij}, 0), & i \neq j, \\ \sum_k \max(v_{ik}, 0) & i = j. \end{cases}$$

The structure of this matrix will be a key component in our discussion of the dynamics of the system (4)–(5). To analyse its structure, we introduce the directed graph formed by considering grid cells as vertices and the fluxes v_{ij} as directed edges.

In general, the dynamics of the incompressible two-phase system is driven by three different mechanisms. To see this, we first use the fundamental theorem of vector calculus to introduce a Helmholtz decomposition of the total Darcy velocity; that is, we write the velocity as a sum of an irrotational (curl-free) vector field and a solenoidal (divergence-free) vector field, $\vec{v} = \vec{v}_{irr} + \vec{v}_{rot}$. In our model, the irrotational and the solenoidal velocities satisfy the following pressure equations

$$(8) \quad \nabla \cdot \vec{v}_{irr} = q, \quad \vec{v}_{irr} + \lambda \mathbf{K} \nabla p_{irr} = 0$$

$$(9) \quad \nabla \cdot \vec{v}_{rot} = 0, \quad \vec{v}_{rot} + \lambda \mathbf{K} \nabla p_{rot} = \lambda \mathbf{K} (\lambda_w \rho_w + \lambda_n \rho_n) \vec{g}.$$

We will later come back to how the two vector fields in the decomposition can be computed efficiently.

Introducing the irrotational and the solenoidal velocities in the transport equation, we obtain the following equation

$$(10) \quad \phi \partial_t S_w + \nabla \left[f_w(S) \vec{v}_{irr} + f_w(S) \vec{v}_{rot} + f_w(S) \lambda_n(S) (\rho_w - \rho_n) \mathbf{K} \vec{g} \right] = q_w,$$

from which we see that there are three different contributions to the flux: The first term, $f_w(s) \vec{v}_{irr}$, represents pure viscous forces driven by the gradient of a potential. If this is the only flux contribution, the transport equation (10) will have a unidirectional flow property (or causality principle) which ensures that perturbations travel along irrotational streamlines from fluid sources or inflow boundaries to fluid sinks or outflow boundaries. If the fluxes are computed from (8) using a monotone method, no streamlines will reenter a grid cell they have passed through earlier. Likewise, the directed flux graph will be acyclic and can be flattened by a topological sort. Using this reordering, the upwind flux matrix can be rearranged to a lower triangular form by a symmetric permutation of the rows and columns using Tarjan’s algorithm [10]. Hence, the nonlinear system (6) can be computed using a highly efficient by nonlinear Gauss–Seidel approach, in which the solution is computed cell-by-cell using e.g., Ridder’s method, see [27] for more details.

The second term, $f_w(S) \vec{v}_{rot}$, represents the gravity-induced advection, which has a circular behavior similar to convection in heat conduction. When \vec{v}_{rot} is nonzero, the total velocity will no longer be irrotational, which, in the worst case, means that streamlines may reenter a cell they have passed through earlier and hence increase the implementational complexity of a streamline method. Likewise, the directed flux graph will generally not be acyclic and may contain cycles that contain cells that have a circular dependence in (6). The cycles are easy to detect using a topological sort of the reverse flux graph and once they are detected, the nonlinear system can be rearranged into a block-triangular form with circularly dependent cells appearing as matrix blocks on the diagonal. Also in this case, it may be advantageous to solve (6) using a nonlinear Gauss–Seidel algorithm, but the efficiency of the approach will now depend on the size and the number of matrix blocks that must be solved using a Newton–Raphson type method. The rotational (solenoidal) contribution to the total velocity depends upon the saturation distribution, and the larger this

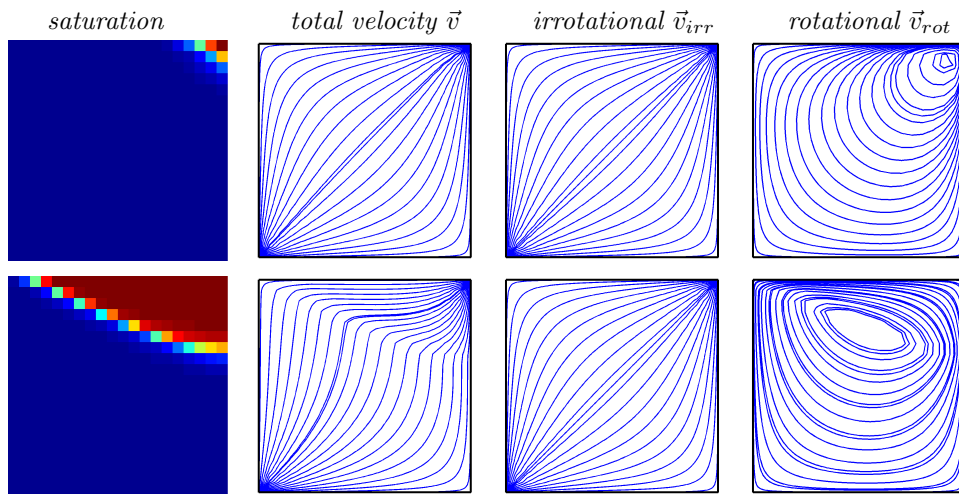


FIGURE 1. Buoyancy dominated flow in a homogeneous domain with a light fluid injected into a heavy fluid from the upper-right corner. The upper plots show the solution after one day and the lower plots the solution after twenty days.

contribution is, the tighter the coupling will be between the flow and the transport equation.

The third flux term in (10) represents gravity segregation that acts along one-dimensional lines parallel to the gravity vector \vec{g} . Along each such gravity line, the characteristics will generally point in both directions corresponding to the lighter fluid moving upwards and the heavier fluid moving downwards. In streamline and other related methods, the gravity step is therefore typically accounted for in a separate step [17, 16, 6, 3]. We will come back to such operator splittings in the next section. First, however, we consider an example that illustrate the irrotational and rotational parts of the dynamics.

Example 1. *We consider the evolution of two fluids with density 100 and 1000 Kg/m^3 , linear relative permeability curves, and viscosity 1 cP for both fluids. The domain is homogeneous with permeability 100 mD covering the unit square. In the upper-right corner, a fluid source injects the lighter fluid at a rate of $0.01\text{m}^3/\text{day}$, whereas fluid is produced at the same rate from a sink in the lower-left corner. Initially, the saturation of the light fluid is zero in the whole domain. The injection of fluid result in a flow that is driven by a linear combination of buoyancy forces and a pressure gradient, but with a strong buoyancy dominance. Figure 1 shows the saturation field and the Helmholtz decomposition of the total Darcy velocity. We observe that the strength of the solenoidal component increases as more light fluid enters the domain.*

Let us now reverse the flow and inject the light fluid in the lower-left corner and produce fluids from the upper-right corner. Moreover, to increase the influence of gravity we reduce the injection rate to $0.001\text{m}^3/\text{day}$. Figure 2 shows the saturation field, the total velocity, the solenoidal velocities, and the cells that are part of a cycle in the directed graph and hence mutually dependent after twenty, one hundred, and three hundred days. (The irrotational velocity is identical to the one shown in Figure 1 and is therefore not plotted.) Here, the advective flow that is imposed by the source-sink pair is so weak that the flow is almost fully segregated. A sharp

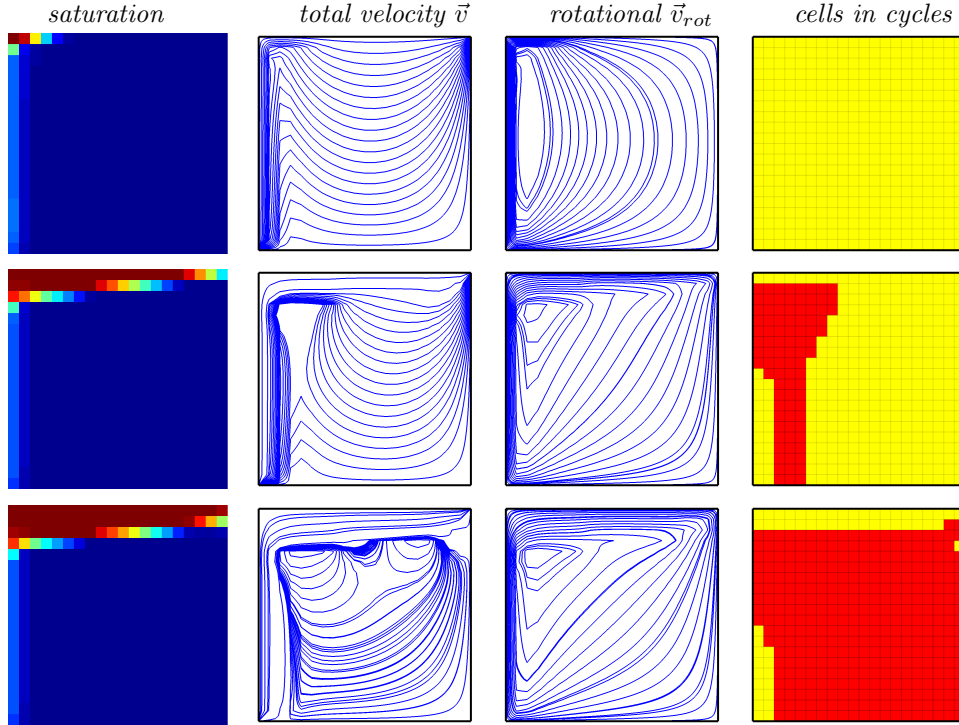


FIGURE 2. Buoyancy dominated flow in a homogeneous domain with a light fluid injected into a heavy fluid from the lower-left corner. The plots show the solution after twenty, one hundred, and three hundred days (from top to bottom). In the left column, cells involved in a cycle are colored red whereas cells that can be computed independently in sequence are colored yellow.

interface forms between the fluids with a corresponding jump in density that yields a strong solenoidal contribution to the total velocity field. As a result, we observe that large irreducible blocks form when the light fluid accumulates at the top boundary. After 100 days, 89 of 400 grid cells are connected in one irreducible diagonal block. This will significantly reduce the efficiency of a nonlinear Gauss–Seidel method. After 300 days, there are two irreducible blocks with 341 grid cells in one and 4 in the other.

The purpose of the example above was to show the impact the rotational part of the velocity field may have on the efficiency of streamline methods and single-point upwind schemes using reorder techniques to accelerate computations. The appearance of loops and spirals in the velocity field is inconvenient when tracing streamlines, e.g., because one often ends up discarding such streamlines. This makes the solution of transport along such streamlines in regions dominated by gravity unappealing. Single-point upwind schemes accelerated with a nonlinear Gauss–Seidel solver based upon optimal ordering is a promising technique to improve the effectiveness and robustness of implicit transport schemes. However, like for the streamline methods, the efficiency of this method is reduced when there are large loops in the velocity field, for which all the corresponding unknowns in (6) must be solved for simultaneously. In fact, since optimal ordering is based on a reduction

of the flux matrix \mathbf{V} in (6) to (block)-triangular form using a topological sorting algorithm [27, 28, 10], the algorithm is sensitive to small reverse fluxes that are caused by gravitational effects.

In the next section, we will use the insight developed above to set up efficient operator-splitting methods for (4)–(5).

3. Operator-splitting methods

A common approach for solving (4)–(5) is to use a sequential splitting in which one fixes the saturation in the pressure equation (4) and solves for the unknown pressure and velocities/fluxes, which are subsequently held fixed when evolving the saturations a time step Δt according to (5). If necessary, the two steps can be repeated before the method moves on to the next time step. Many numerical methods involve a further operator splitting of (5). The primary example is streamline simulation, which splits the equation into an advective and a gravity segregation part [17, 16, 6, 3]

$$(11) \quad \phi \partial_t S + \nabla \cdot (f_w(S) \vec{v}) = q_w,$$

$$(12) \quad \phi \partial_t S + \nabla \cdot [f_w(S) \lambda_n(S) (\rho_w - \rho_n) \mathbf{K} \vec{g}] = 0,$$

If we let \mathcal{A}_{adv} and \mathcal{A}_{seg} denote the corresponding operators, approximate solutions of (5) can be constructed using the following operator splitting:

$$(13) \quad S(t + \Delta t) \approx \left[(\mathcal{A}_{seg}(\Delta t/n))^n (\mathcal{A}_{adv}(\Delta t/m))^m \right] S(t),$$

where m and n are two positive numbers (in most cases $n \leq m = 1$).

To numerically approximate \mathcal{A}_{adv} and \mathcal{A}_{seg} , we note that each of these two equations (11) and (12) can be decomposed into a family of one-dimensional transport equations along curves in three-dimensional space (streamlines and gravity lines, respectively) given by

$$(14) \quad \frac{d\vec{x}}{d\tau} = \frac{\vec{v}(\vec{x})}{\phi(\vec{x})} \quad \text{and} \quad \frac{d\vec{x}}{dr} = \frac{\vec{g}}{|\vec{g}|}.$$

The advection equation (11) has only positive characteristics (also for more complex models with more than two phases and/or components) and can usually be computed quite efficiently using Lagrangian coordinates: the single-point upwind method, for instance, gives a nonlinear triangular system with only one nonzero subdiagonal when applied along streamlines, or one can use a highly efficient and unconditionally stable front-tracking method [18]. Using streamlines involves a mapping from Eulerian to Lagrangian coordinates and back again, which may introduce numerical dissipation and lack of mass conservation [21]. To guarantee mass conservation, one may alternatively work directly in Eulerian coordinates and exploit the causality of (11) to solve the standard single-point upwind method (6) using a nonlinear, block-based Gauss–Seidel method, as discussed in the previous section.

The segregation equation (12) has both positive and negative characteristics along gravity lines and will in most cases also have a spatially discontinuous flux function. In reservoir simulation, the standard approach is to use a so-called mobility-weighted upwind flux approximation, in which the upwind direction is determined independently for the two phase mobilities. This discretization is not always correct for discontinuous \mathbf{K} ; fortunately, the correct Godunov method is only slightly more complicated [26]. Alternatively, one can use an unconditionally stable front-tracking method for problems with spatially discontinuous flux [15].

In the previous section, we argued how the presence of rotational components in the total velocity will reduce the efficiency of the nonlinear Gauss–Seidel method for the advective part. Likewise, loops or spirals will complicate tracing of streamlines as well as setting appropriate boundary conditions for the one-dimensional transport equations along each streamline. To remedy these problems, and to accommodate that the gravity segregation and the irrotational and solenoidal advection may occur on different time scales, we split the advection into two sub-equations

$$(15) \quad \phi \partial_t S + \nabla \cdot (f_w(S) \vec{v}_{irr}) = q_w,$$

$$(16) \quad \phi \partial_t S + \nabla \cdot (f_w(S) \vec{v}_{rot}) = 0,$$

If we let \mathcal{A}_{irr} and \mathcal{A}_{rot} denote the corresponding operators, approximate solutions of (5) can be constructed using the following three-step operator splitting:

$$(17) \quad S(t + \Delta t) \approx \left[(\mathcal{A}_{seg}(\Delta t/n))^n (\mathcal{A}_{rot}(\Delta t/m))^m (\mathcal{A}_{irr}(\Delta t/\ell))^\ell \right] S(t),$$

where m , n , and ℓ are three positive numbers. The main points of (17) are that: (i) each subequation is solved using an optimal scheme with an optimal time step, and (ii) the rotational part of the velocity is removed from the advective velocity to enable the use of highly efficient schemes available for irrotational flows. There are, of course, many other ways to sequence the operators to better preserve the interaction of the three physical mechanisms. For instance, the order of \mathcal{A}_{seg} and \mathcal{A}_{rot} can be interchanged or the operators can be combined if one does not want to exploit the one-dimensional structure of (12).

The operator splitting (17) assumes that the pressure equation is solved twice with different right-hand sides (see (8) and (9)). Fortunately, this is not twice as expensive as solving (4). First of all, we only have to generate the system matrix once. Furthermore, any preconditioning or factorization of the system matrix may be reused for the second pressure solve. It is also worth noting that the coupling between the pressure equation and the saturation equation through saturation-dependent mobilities can be quite severe in regions where the flow is dominated by gravitational effects. In these regions, the velocity field changes as fast as the saturation fronts move. By splitting the velocity field in an irrotational part and a rotational part, we can quantify the degree with which the gravitational effects induce tighter coupling in the operator splitting.

4. Numerical experiments

In this section, we will present numerical experiments that illustrate the use of operator splitting, as well as the importance of understanding the dynamics of the problem when applying operator splitting.

The emphasis of our first example is to illustrate how the timescales of the different physical effects that contribute to the overall flow dynamics are affected by heterogeneous and anisotropic permeability fields.

Example 2. *We consider a vertical cross-section of a reservoir described by a 220×85 Cartesian grid with petrophysical parameters sampled from the first x - z slice of Model 2 from the SPE 10 benchmark [?]. Using this model, we will show that the relative importance of different parts of the flow dynamics depend on the heterogeneity of the permeability field in a manner that is hard to predict by inspection. The reservoir is initially filled with a heavy fluid with density 1000 Kg/m^3 into which a light fluid with density 100 Kg/m^3 is injected at a constant rate of one pore volume per 20 000 days from a source evenly distributed in the grid cells at the left boundary. On purpose, the density difference is large and the injection*

TABLE 1. The maximal time step in hours for an explicit method for different parts of the dynamics of the transport equations for the two models of Example ??.

| Model | Time (years) | Irrotational | Rotational | Segregation |
|-------------|--------------|--------------|------------|-------------|
| isotropic | 5 000 | 5.0 | 89 | 0.23 |
| | 10 000 | 5.0 | 95 | 0.48 |
| anisotropic | 5 000 | 24 | 7 700 | 0.75 |
| | 10 000 | 31 | 7 000 | 0.75 |

rate is small to exaggerate the effects of gravity. Reservoir fluids are produced by a sink evenly distributed in the cells along the right boundary. The fluid mobilities are specified using Corey-type relative permeabilities with exponent 2 and a viscosity of 1 centi Poise for both fluids. For simplicity, we set gravity to 10 m/s². For the porosity, we use a lower cut-off value of 10⁻³.

We present two simulations: the first is isotropic and uses only the x-permeability from the original model, whereas the second uses the original, anisotropic permeability field from [?]. Figure ?? shows the saturation field for the isotropic model after 5 000 and 10 000 days, as well as a streamline plot of the total velocity field and a plot of cells that belong to strongly connected components (or loops) in the corresponding directed flux graph. We can see that the velocity field is quite irregular and that the local direction of flow changes with time. This is reflected in the plot of loops in which the locations of the strongly coupled cells seem to follow the saturation fronts. It is worth noting that for a loop to appear in the total velocity, the strength (or timescale) of the irrotational advection and the solenoidal advection must be of the same magnitude, locally. For high injection rates, however, we expect that the irrotational advection will have a shorter timescale than the solenoidal advection for the domain as a whole. The timescales for the different parts of the dynamics are reported in upper part of Table ??.

In Figure ??, we show the same simulation results for the anisotropic model. In this case, the vertical permeability is significantly smaller than the horizontal permeability; more than half of the cells have a large K_x -to- K_z anisotropy ratio (in the range of 10⁴), which presumably models shale layers. This is reflected in a total velocity less affected by gravity, with fewer and smaller loops. In the lower part of Table ??, we report the timescales of this simulation. We see that the timescale of segregation is only slightly increased by the reduced vertical communication; this timescale is determined roughly by the density difference, fluid viscosity, and the largest z-permeability. The timescale for the solenoidal advection, on the other hand, is significantly increased because of the shale layers that dramatically decreases the effective permeability along any closed streamline. As a consequence, the number of loops in the total velocity field is reduced; it is unlikely that the local timescales for irrotational advection and solenoidal advection are of the same magnitude. However, we remark that in a three-dimensional model, where the pressure gradient and velocity will decrease with distance from the wells, these timescales will likely be of the same magnitude even in the presence of small z-permeability.

The emphasis of our next example is to demonstrate that the new gravity splitting we proposed in the previous section is applicable to realistic reservoir models with complex, twisted, and deformed grid cells; sealing and partially sealing faults; thin and eroded layers; barriers, etc.

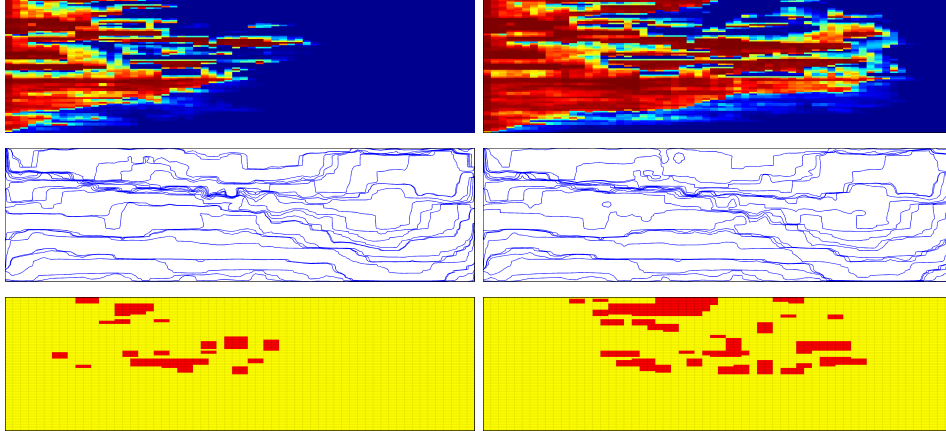


FIGURE 3. Constant rate injection in all layers of a vertical cross-section with *isotropic* permeability. The plots show the saturation of the injected fluid (top), streamlines of the total velocity (middle), and the strongly connected grid cells in red (bottom) at 5 000 days (left) and 10 000 days (right).

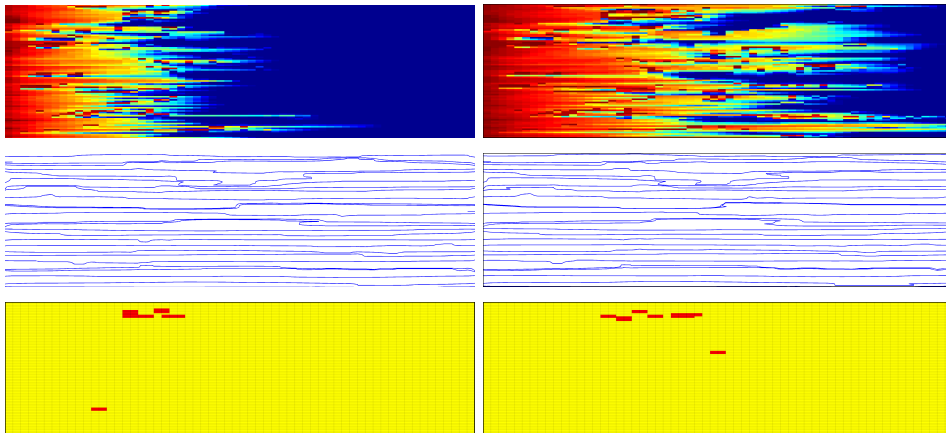


FIGURE 4. Constant rate injection in all layers of a vertical cross-section with *anisotropic* permeability. The plots show the saturation of the injected fluid (top), streamlines of the total velocity (middle), and the strongly connected grid cells in red (bottom) at 5 000 days (left) and 10 000 days (right).

Example 3. *The model in this example is based on a real-field model from offshore of Norway. We use the original geology and reservoir geometry, described as a corner-point grid with approximately 44 000 active cells, but have modified the fluids and wells. We have filled the original gas cap with oil to make the model more suitable for an incompressible formulation. Initially, the reservoir is in near hydrostatic equilibrium with the original oil-water contact preserved. We inject water in some of the original wells. Furthermore, we use Corey relative permeability curves*

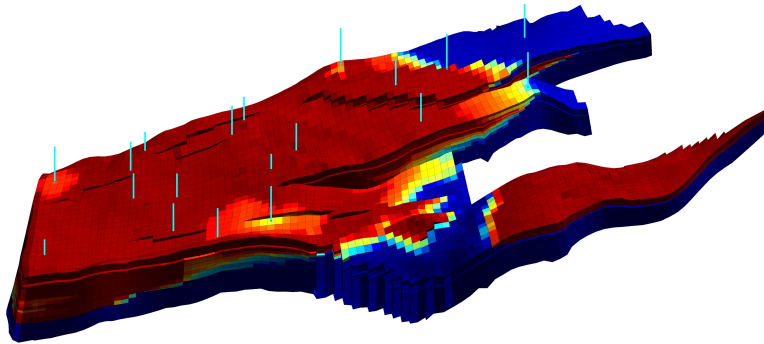


FIGURE 5. Realistic reservoir model from offshore Norway. The plot shows the saturation field after ten years of water injection, computed using equally-spaced pressure steps of length 2.5 years.

TABLE 2. Estimated time step restrictions for each of the splitting steps (15), (16), and (12) for the model shown in Figure 3.

| Time (years) | 0.25 | 0.5 | 0.75 | 1.0 | 1.25 | 2.5 | 5.0 | 7.5 |
|----------------------------|------|-----|------|-----|------|-----|-----|-----|
| \mathcal{A}_{irr} (days) | 1 | 1 | 1 | 1 | 1 | 1 | 1 | 1 |
| \mathcal{A}_{rot} (days) | 46 | 79 | 82 | 85 | 87 | 120 | 200 | 213 |
| \mathcal{A}_{seg} (days) | 6 | 6 | 6 | 6 | 6 | 6 | 6 | 6 |

with Corey exponent 4 and viscosities 0.318 cP and 1 cP for oil and water, respectively. The density difference used is 174 kg. Figure 3 shows the water saturation after ten years of injection.

Our first object of interest is the timescales associated with gravity segregation and irrotational and rotational advection. Table 1 reports the maximum time step fulfilling a CFL restrictions for the three substeps. We see that the irrotational advection step has the most severe time-step restriction, whereas the maximal time steps for the gravity segregation and rotational advection are one and two orders of magnitude higher, respectively. The time restriction for the rotational step increases with time, but seemed to stabilize around 200 days for longer times. The table also shows that with a maximum time step of six days, an explicit method would be feasible for the segregation step. Likewise, a value of one day for the advection step is, at least in our opinion, close to acceptable for the (irrotational) advective step. The model resolution is quite coarse, in particular near the wells, and a further lateral refinement in the near-well regions would worsen the restriction on the advective step, but not affect the gravity step significantly.

Next, we consider the possibility of accelerating implicit temporal discretizations using a nonlinear Gauss-Seidel method. As a measure of the complexity of the nonlinear problem, we report some statistics on the cycles that appear in the flux graph, or more precisely, the number and size of the irreducible diagonal blocks in the upwind flux matrix \mathbf{V} from (7). The irreducible blocks are identified by permuting \mathbf{V} to a block-diagonal form using Tarjan's algorithm [10]. Table 2 reports the number of cycles, the number of cells in the largest cycle, and the total number of cells involved in cycles observed for two different sizes of the pressure step. These quantities give a good picture of the difficulties of the nonlinear problem which would ultimately limit the efficiency of implicit methods for long time steps. If the flux is computed using a monotone two-point flux-approximation scheme, there are

TABLE 3. Number of cycles (N), number of cells in the largest cycle (max), and the total number of cells involved in cycles for the model in Figure 3 for fluxes computed with a two-point method with pressure steps Δt equal 2.5 and 0.25 years.

| Δt years | Time years | \vec{v}_{rot} | | | $\vec{v} = \vec{v}_{irr} + \vec{v}_{rot}$ | | |
|---------------------|---------------|-----------------|-------|--------|---|-----|--------|
| | | N | max | #cells | N | max | #cells |
| 2.5 | 2.5 | 26 | 37835 | 38133 | 18 | 188 | 410 |
| | 5 | 27 | 38912 | 39390 | 10 | 178 | 356 |
| | 7.5 | 13 | 39913 | 40820 | 15 | 186 | 404 |
| 0.25 | 0.25 | 9 | 31709 | 32489 | 34 | 443 | 728 |
| | 1.0 | 8 | 36763 | 36920 | 22 | 202 | 594 |
| | 2.0 | 9 | 37856 | 38002 | 19 | 195 | 563 |
| | 2.25 | 9 | 38092 | 38246 | 20 | 193 | 570 |

TABLE 4. Number of cycles (N), number of cells in the largest cycle (max), and the total number of cells involved in cycles for the model in Figure 3 for fluxes computed with a mimetic method with pressure step of 0.25 years.

| Time years | \vec{v}_{irr} | | | \vec{v}_{rot} | | | $\vec{v} = \vec{v}_{irr} + \vec{v}_{rot}$ | | |
|---------------|-----------------|------|--------|-----------------|-------|--------|---|------|--------|
| | N | max | #cells | N | max | #cells | N | max | #cells |
| 0.25 | 424 | 3314 | 9038 | 98 | 33451 | 35314 | 453 | 2245 | 8697 |
| 0.50 | 433 | 3268 | 9514 | 76 | 36277 | 37720 | 423 | 3274 | 10272 |

no cycles in the flux field corresponding to \vec{v}_{irr} , whereas the total velocity has 400–500 cells involved in cycles. The solenoidal velocity, on the other hand, has cycles covering almost the complete domain.

In general, having as few cycles as possible is highly favorable when using a streamline method or a reordering, nonlinear Gauss–Seidel method to accelerate the advective step. So far, we have only considered a two-point scheme for solving the pressure equation(s). It is well-known that this scheme is inconsistent and hence ill-suited for rough geometries or strongly anisotropic permeability tensors. If one, on the other hand, uses a convergent scheme, such a multipoint or mimetic method, one will inevitably obtain flux field with cycles, even without gravity as for \vec{v}_{irr} in (8). There seems to be a close relation between cycles in the velocity field and monotonicity of the pressure, see e.g., Figure 7 in [23]. Unfortunately, there exists no (convergent) monotone method with local stencil that guarantees monotone pressure [20]. On the other hand, our experience is that non-convergent, monotone methods guarantee loop-free velocity fields. In Table 3 we have report the same statistics as in Table 2 for the flux computed by a mimetic scheme from (8). In this case, the number of cycles produced by the mimetic scheme is approximately the same as the the number of cycles introduced by the solenoidal contribution in Table 2.

Based on the combined results reported in Tables 1 and 2, a good operator-splitting approach would be to use (17), solving (15) implicitly to approximate \mathcal{A}_{irr} and (16) explicitly to approximate \mathcal{A}_{rot} . In the following, we present a simplified analysis that indicates that this observation may indeed be valid for many other cases. We start by considering the segregation step, where the maximal time step

allowed by the CFL condition is given by

$$(18) \quad t_{seg} \sim \Delta z / \left(K_z |\vec{g}| \Delta \rho \frac{d}{dS} [\lambda_o(S) f_w(S)] \phi \right)$$

Here $\Delta \rho$ is the difference in densities and K_z is the vertical permeability. The solenoidal step depends upon the particular distribution of the fluid which decides the gravity-driven contribution of the total velocity. A useful estimate of the fluid distribution can be derived based upon the Dupuit approximation which is commonly used in vertical-equilibrium models [4, 25, 7]. Assuming that the light fluid is confined to a thin layer of height h under a horizontal top surface of the aquifer gives the following time step due to motion in the x direction,

$$(19) \quad t_{rot}^x \sim \Delta x / \left(K_x |\vec{g}| \frac{\Delta \rho}{\mu} \frac{\partial h}{\partial x} \phi \right),$$

where K_x is the lateral permeability (in the x -direction) and μ is the viscosity of the light fluid. From the same equation we can find the maximal time step associated with vertical flow

$$(20) \quad t_{rot}^z \sim \Delta z / \left(K_x |\vec{g}| \frac{\Delta \rho}{2\mu} \frac{\partial^2 h^2}{\partial x^2} \phi \right).$$

The ratio between these two estimates is

$$(21) \quad t_{rot}^x / t_{rot}^z \sim \Delta x \frac{\partial^2 h^2}{\partial x^2} / \left(2 \Delta z \frac{\partial h}{\partial x} \right) \sim \frac{\Delta x H}{\Delta z L}.$$

Here, H denotes a typical vertical length scale while L denotes a horizontal length scale. For most reservoir models, in which the number of grid cells used to resolve the lateral variation is larger than the number of cells used in the vertical direction, this ratio would be greater than one. We also notice that this ratio does not depend on K_z . The ratio of the segregation step to the rotational step is

$$(22) \quad t_{seg} / t_{rot}^x \sim K_x \Delta z \frac{\partial h}{\partial x} / \left(K_z \Delta x \frac{d}{dS} [\lambda_o f_w] \mu \right) \sim \frac{\Delta z K_x H}{\Delta x K_z L}.$$

If we assume that $K_x / K_z \sim 10$, $\Delta x / \Delta z$ is in the range 50–100, and that $H / L \sim 100$, the ratio will be between 0.1 and 0.2. In Table 1 of Example 2, we observed that the ratio is 0.1, or less, which suggests that the rotational velocity for many models can be treated explicitly. When this is the case, the convection step will be relatively inexpensive to compute compared to the advection and segregation steps. (A similar scaling would be expected also in cases for which the Dupuit approximation is not valid because the length scale of the lateral variation in most cases are longer than the vertical scale of a reservoir.)

In the previous example, we considered a real model of a petroleum reservoir having dynamics dominated by viscous forces (injection and production wells). In the next example, we will consider another real-life example which is dominated by gravity segregation.

Example 4. *The Johansen formation is a deep saline aquifer in the North Sea which is evaluated as a potential storage for CO_2 in a future pilot project for CCS at Mongstad, Norway. The model has been studied recently by several authors [13, 5], and is available online (see Eigestad et al. [12]). We consider the sector model 'NPD5' consisting of the lower three geological zones of Johansen, which covers an area of approximately $50 \times 50 \text{ km}^2$. This model was used for simulations by Eigestad et al. [13]; the left plot in Figure 4 shows a height-map of the sector model with an injection well indicated.*

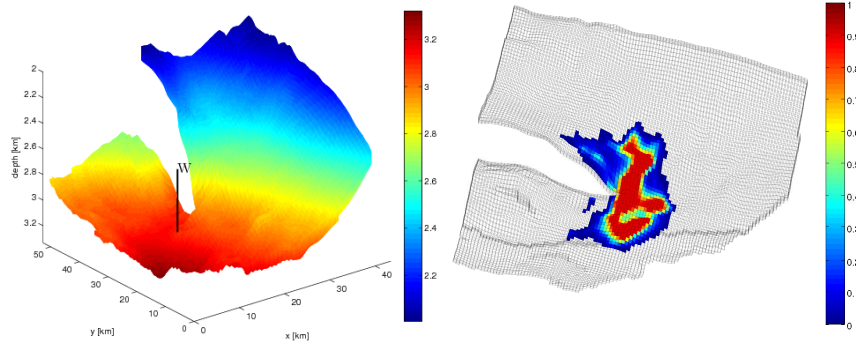


FIGURE 6. The Johansen model. The left plot shows a height map of the top surface, whereas the right plot shows the CO_2 distribution 500 years after the injection start.

TABLE 5. The maximal time step in years for an explicit method for different parts of the dynamics of the transport equations for the Johansen formation for the 3D model in (4)–(5) and the vertical equilibrium (VE) model in (23)–(24).

| Model | Time | Advection | Rotation | Segregation | Parabolic |
|-------|----------------|-----------|----------|-------------|-----------|
| 3D | injection | 0.1 | 10 | 0.04 | — |
| | post injection | — | 12 | 0.04 | — |
| VE | injection | 1 | 201 | 8 | 6 |
| | post injection | — | 164 | 8 | 3 |

The simulation setup is as follows: 3.5 Mt of CO_2 is injected yearly for 110 years, and we study the migration for a post-injection period of 390 years. We use a fluid model similar to what was used in the previous study on Johansen [13]. The fluid properties are reference values for CO_2 and brine taken at 300 bar. At this pressure, the approximate viscosity and density of supercritical CO_2 are 0.057 cP and 686.54 kg/m^3 , respectively, while for brine the viscosity and density are 0.30860 cP and 975.86 kg/m^3 . Residual trapping is accounted for by setting the residual saturation of 0.2 for CO_2 and 0.1 for brine. The right plot shows the CO_2 distribution 500 years after the start of the injection.

The upper half of Table 4 reports representative maximal time steps for the (irrotational) advection, the rotational advection, and the gravity segregation. During the injection period, the dynamics of the problem is dominated by the interplay of irrotational advection and gravity segregation, i.e., as in the upper plots of Figure 2 in Example 1. Because of the large density difference between the injected CO_2 and the resident brine, the time constant is lower for the gravity segregation than for the viscous (irrotational) advection. Still, the operator splittings (13) and (17) are quite applicable, using either streamlines or a 3D finite-volume method with a nonlinear Gauss-Seidel solver for the advective part.

When injection is terminated, the viscous advection disappears, leaving the rotational advection and gravity segregation as the main effects. Because of the large disparity in time constants, it does not make sense to apply an operator splitting. Instead, one can as a good approximation assume that the gravity segregation

reaches vertical equilibrium instantaneously, as in the Dupuit approximation discussed above. This means that the flow of a layer of CO_2 can be approximated in terms of its thickness to obtain a 2D simulation model.

The vertical-equilibrium (VE) formulation for (4)–(5) can be written in a standard fractional flow formulation as a system of a pressure equation and a transport equation as follows:

$$(23) \quad \nabla_{\parallel} \cdot \vec{v} = q_{\text{tot}}, \quad \vec{v} = -\lambda_t \left[\nabla_{\parallel} p_t - (f_v \rho_{CO_2} + [1 - f_v] \rho_w) \vec{g}_{\parallel} + \frac{\lambda_w}{\lambda_t} \nabla_{\parallel} g_c \right]$$

$$(24) \quad \frac{\partial s}{\partial t} + \nabla_{\parallel} \left(f_v(s, x) \vec{v} + f_g(s, x) [\vec{g}_{\parallel} + \nabla_{\parallel} g_c(s, x)] \right) = q(x)$$

Here, s is the ratio between the height of the CO_2 column h and the total formation height H , p_t is the pressure along the top surface, and subscripts \parallel and \perp denote parallel to and perpendicular to the top surface. Moreover, to illuminate the similarity with the standard two-phase flow model, we introduce pseudo mobilities, fractional flows, and 'capillary terms' given by

$$(25) \quad \lambda_{CO_2}(s, x) = \int_0^{sH} k_{CO_2}(1) K_x(z, x) dz, \quad \lambda_w(s, x) = \int_{sH}^H k_w(1) K_x(z, x) dz,$$

$$f_v(s, x) = \frac{\lambda_{CO_2}(s, x)}{\lambda_{CO_2}(s, x) + \lambda_w(s, x)}, \quad f_g(s, x) = \lambda_w(s, x) f_v(s, x),$$

$$g_c(s, x) = s(\rho_{CO_2} - \rho_w) g_{\perp}.$$

As in (8) and (9), the pressure equation (23) can be decomposed into irrotational and solenoidal subequations. Likewise, the flux terms in (24) can be separated into viscous advection, rotational forces, gravity segregation, and a parabolic 'capillary' term. The corresponding time constants are reported in the lower half of Table 4.

Comparing the upper and lower parts of Table 4 shows why vertical equilibrium simulations may be attractive to increase (lateral) resolution while saving computational cost. Although this approach reduces the dimension of the model, important information of the heterogeneities in the underlying 3D medium is preserved. Indeed, in many cases the errors resulting from the VE assumption may be significantly smaller than the errors introduced by the overly coarse resolution needed to make the 3D simulation model computationally tractable. A more thorough discussion of VE simulations of the Johansen formation is given by Ligaarden and Nilsen [24].

5. Concluding remarks

In this paper we have analysed the dynamics of a simple two-phase model and shown that it is governed by three different physical mechanisms: (irrotational) viscous advection, rotational (gravity-induced) advection, and gravity segregation. All three mechanisms act along curves in three-dimensional space: rotational advection acts along closed curves whereas viscous advection and gravity segregation act along curves that start and terminate at fluid sources/sinks or the boundary of the domain.

Based on our analysis of the dynamics, we have devised a new splitting method where we separate the rotation-free advective transport from the dynamics due to gravity. With the proposed method, it may be possibility to improve gravity splitting schemes that use methods fine-tuned for advective flow, such as streamline methods or methods employing causality-based reordering. In our experiments, we have shown that the proposed splitting isolates the dynamics associated with gravity

in an efficient manner or can be used to analyse the utility of an operator splitting method that seeks to utilize effective advection solvers.

Acknowledgments

This research was funded in part by the Research Council of Norway through grants no. 178013 and 186935.

References

- [1] J. R. Appleyard and I. M. Cheshire. The cascade method for accelerated convergence in implicit simulators. In *European Petroleum Conference*, pages 113–122, SPE 12804, 1982. doi: 10.2118/12804-MS.
- [2] R. Baker. Streamline technology reservoir history matching and forecasting = its success limitations, and future. *JCPT*, 40(4):23–27, 2001.
- [3] R. Batycky, M. J. Blunt, and M. R. Thiele. A 3d field scale streamline simulator with gravity and changing well conditions. *SPE*, 12(4):246–254, 1997.
- [4] J. Bear. *Dynamics of Fluids in Porous Media*. Dover, 1988.
- [5] P. E. S. Bergmo, E. Lindeberg, F. Riis, and W. T. Johansen. Exploring geological storage sites for CO2 from Norwegian gas power plants: Johansen formation. *Energy Procedia*, 1(1):2945 – 2952, 2009. ISSN 1876-6102. doi: 10.1016/j.egypro.2009.02.070.
- [6] F. Bratvedt, T. Gimse, and C. Tegnander. Streamline computations for porous media flow including gravity. *Transp. Porous Media*, 25(1):63–78, oct 1996. doi: 10.1007/BF00141262.
- [7] K. H. Coats, J. R. Dempsey, and J. H. Henderson. The use of vertical equilibrium in two-dimensional simulation of three-dimensional reservoir performance. *Soc. Pet. Eng. J.*, Mar:68–71, 1971.
- [8] A. Datta-Gupta and M. J. King. *Streamline Simulation: Theory and Practice*, volume 11 of *SPE Textbook Series*. Society of Petroleum Engineers, 2007.
- [9] J. Douglas, Jr. and H. H. Rachford, Jr. On the numerical solution of heat conduction problems in two and three space variables. *Trans. Amer. Math. Soc.*, 82:421–439, 1956. ISSN 0002-9947.
- [10] I. S. Duff and J. K. Reid. An implementation of Tarjan’s algorithm for the block triangularization of a matrix. *ACM Trans. Math. Software*, 4(2):137–147, 1978.
- [11] Y. Efendiev and T. Y. Hou. *Multiscale Finite Element Methods*, volume 4 of *Surveys and Tutorials in the Applied Mathematical Sciences*. Springer Verlag, 2009.
- [12] G. Eigestad, H. Dahle, B. Hellevang, W. Johansen, K.-A. Lie, F. Riis, and Ø. E. Geological and fluid data for modelling CO2 injection in the Johansen formation, 2008. <http://www.sintef.no/Projectweb/MatMorA/Downloads/Johansen>.
- [13] G. Eigestad, H. Dahle, B. Hellevang, F. Riis, W. Johansen, and E. Øian. Geological modeling and simulation of CO2 injection in the Johansen formation. *Comput. Geosci.*, 13(4):435–450, 2009. doi: 10.1007/s10596-009-9153-y.
- [14] M. S. Espedal and K. H. Karlsen. Numerical solution of reservoir flow models based on large time step operator splitting algorithms. In *Filtration in porous media and industrial application (Cetraro, 1998)*, volume 1734 of *Lecture Notes in Math.*, pages 9–77. Springer, Berlin, 2000.

- [15] T. Gimse and N. H. Risebro. Solution of the Cauchy problem for a conservation law with a discontinuous flux function. *SIAM J. Math. Anal.*, 23(3):635–648, 1992.
- [16] R. H. J. Gmelig Meyling. Numerical methods for solving the nonlinear hyperbolic equations of porous media flow. In *Third International Conference on Hyperbolic Problems, Vol. I, II (Uppsala, 1990)*, pages 503–517, Lund, 1991. Studentlitteratur.
- [17] R. H. J. Gmelig Meyling. A characteristic finite element method for solving non-linear convection-diffusion equations on locally refined grids. In D. Guerillot and O. Guillon, editors, *2nd European Conference on the Mathematics of Oil Recovery*, pages 255–262, Arles, France, Sept 11-14 1990. Editions Technip.
- [18] H. Holden and N. H. Risebro. *Front Tracking for Hyperbolic Conservation Laws*, volume 152 of *Applied Mathematical Sciences*. Springer-Verlag, New York, 2002. ISBN 3-540-43289-2.
- [19] H. Holden, K. H. Karlsen, K.-A. Lie, and N. H. Risebro. *Splitting methods for partial differential equations with rough solutions: Analysis and MATLAB programs*. EMS Series of Lectures in Mathematics. European Mathematical Society (EMS), Zürich, 2010. doi: 10.4171/078.
- [20] E. Keilegavlen, J. M. Nordbotten, and I. Aavatsmark. Sufficient monotonicity criteria are necessary for control volume methods. *App. Math. Lett.*, 22(8): 1178–1180, 2009. doi: doi:10.1016/j.aml.2009.01.048.
- [21] V. Kippe, H. Hægland, and K.-A. Lie. A method to improve the mass-balance in streamline methods. In *SPE Reservoir Simulation Symposium*, Houston, Texas, U.S.A, 26–28 February 2007. SPE 106250.
- [22] F. Kwok and H. Tchelepi. Potential-based reduced newton algorithm for nonlinear multiphase flow in porous media. *J. Comput. Phys.*, 227(1):706–727, 2007. Doi: 10.1016/j.jcp.2007.08.012.
- [23] K.-A. Lie, S. Krogstad, I. S. Ligaarden, J. R. Natvig, H. M. Nilsen, and B. Skaffestad. Discretisation on complex grids – open source MATLAB implementation. In *Proceedings of ECMOR XII–12th European Conference on the Mathematics of Oil Recovery*, Oxford, UK, 6–9 September 2010. EAGE.
- [24] I. S. Ligaarden and H. M. Nilsen. Numerical aspects of using vertical equilibrium models for simulating CO₂ sequestration. In *Proceedings of ECMOR XII–12th European Conference on the Mathematics of Oil Recovery*, Oxford, UK, 6–9 September 2010. EAGE.
- [25] J. C. Martin. Some mathematical aspects of two phase flow with application to flooding and gravity segregation. *Prod. Monthly*, 22(6):22–35, 1958.
- [26] S. Mishara and J. Jaffré. On the upstream mobility scheme for two-phase flow in porous media. *Comput. Geosci.*, 14(1):105–124, 2010.
- [27] J. R. Natvig and K.-A. Lie. Fast computation of multiphase flow in porous media by implicit discontinuous Galerkin schemes with optimal ordering of elements. *J. Comput. Phys.*, 227(24):10108–10124, 2008. doi: 10.1016/j.jcp.2008.08.024.
- [28] J. R. Natvig and K.-A. Lie. On efficient implicit upwind schemes. In *Proceedings of ECMOR XI, Bergen, Norway, 8–11 September*. EAGE, 2008.
- [29] D. W. Peaceman and H. H. Rachford, Jr. The numerical solution of parabolic and elliptic differential equations. *J. Soc. Indust. Appl. Math.*, 3:28–41, 1955.
- [30] M. Thiele. Streamline simulation. In *8th International Forum on Reservoir Simulation*, Stresa / Lago Maggiore, Italy, 20–24 June 2005.

SINTEF, Department of Applied Mathematics, PO Box 124 Blindern, NO-0314 Oslo, Norway
E-mail: {Knut-Andreas.Lie, Jostein.R.Natvig, Halvor.M.Nilsen}@sindef.no
URL: <http://folk.uio.no/kalie>